Solid State Ionics 403 (2023) 116408

Contents lists available at ScienceDirect

Solid State Ionics

journal homepage: www.elsevier.com/locate/ssi

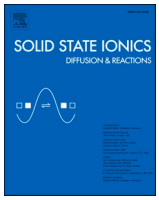

Liquid phase penetration sintering of garnet-type solid electrolyte LLZTO

Naoki Yoshida, Naoaki Kuwata *, Gen Hasegawa, Kazunori Takada

Center for Green Research on Energy and Environmental Materials, National Institute for Materials Science (NIMS), 1-1 Namiki, Tsukuba, Ibaraki 305-0044, Japan

ARTICLE INFO

Keywords:
Solid electrolyte
Liquid phase
$Li_7La_3Zr_2O_{12}$ garnet
$LiOH{\cdot}H_2O$
Low-temperature sintering

ABSTRACT

Developing processes for manufacturing all-solid-state batteries that form ionic–conductive interfaces at low temperatures is crucial. In this study, dense ceramics garnet-type lithium ionconductors, $Li_{6.5}La_3Zr_{1.5}Ta_{0.5}O_{12}$ (LLZTO) were prepared at low temperatures (500–800 °C) by reactive liquid phase penetration sintering (LPPS). In this process, pressed precursor oxides ($La_3Zr_{1.5}Ta_{0.5}O_{8.75}$) were exposed to the melt of lithium hydroxide monohydrate ($LiOH{\cdot}H_2O$). The garnet-type lithium ion conductor prepared by LPPS at 800 °C exhibited a total lithium ion conductivity of 2×10^{-4} S cm^{-1} at 25 °C. The prepared sample has a garnet crystalline network structure containing amorphous LiOH. The activation energy required for lithium-ion conduction of LLZTO prepared by the LPPS method (0.41 eV) is consistent with that of samples prepared by the conventional solid-phase sintering method at higher temperatures.

1. Introduction

Garnet-type lithium ion conductor, $Li_{6.5}La_3Zr_{1.5}Ta_{0.5}O_{12}$ (LLZTO), is a solid electrolyte for all-solid-state batteries due to its high total (bulk and grain boundary) lithium ion conductivity of 10^{-4} S cm^{-1} at 25 °C, and good chemical stability against lithium metal [1–6]. Usually, a sintering temperature above 1100 °C is required to prepare dense LLZTO pellets with high ionic conductivity using the solid phase sintering (SPS) method [3]. However, high-temperature sintering during the fabrication of solid-state batteries often promotes reactions between the electrolyte and electrode, forming highly resistive reaction products at the interface [7–18]. Therefore, a low-temperature sintering method is required for LLZTO to avoid the formation of a resistive interface and to realize solid-state batteries.

Liquid-phase sintering (LPS) effectively produces dense ceramics at low temperatures. The addition of a sintering aid, which forms a liquid phase at the sintering temperature, promotes densification and particle growth at low temperatures [19]. Li-Al-O produced by adding Al_2O_3 or by diffusion from an alumina crucible is a well-known liquid phase for achieving $Li_7La_3Zr_2O_{12}$ (LLZO) densification [20–26]. The Li-Al-O-liquid phase, which promotes the grain growth of LLZO particles at high temperatures, was produced at 1055 °C [20–29]. LLZO reacts in the atmosphere to form Li_2CO_3. Li_2CO_3 also acts as a liquid phase, and the ceramics shrink because of the compressive capillary force near the melting point [30]. Moreover, the addition of glass-forming materials such as $LiPO_3$, Li_3BO_3, Li_2O-Al_2O_3-SiO_2, and LiOH is effective for grain growth because of liquid-phase formation at low temperatures [31–36]. In particular, adding an appropriate amount of Li_3BO_3 promotes grain growth in LLZTO particles [34,37–39]. Tadanaga et al. achieved a lithium-ion conductivity of 1×10^{-4} S cm^{-1} by adding Li_3BO_3 to Al-doped LLZO and sintering it at 900 °C [38]. However, excessive addition of Li_3BO_3 prevents contact between the LLZO particles owing to the aggregated liquid phase [40]. Although the temperature required to prepare LLZO pellets is 1100 °C for SPS, this temperature can be approximately 900 °C for LPS [41]. Table 1 summarizes the previous reports on the preparation of LLZO pellets using LPS.

Low temperature synthesis of LLZO powder is possible at 700–800 °C using the sol-gel method [35,42–47]. Kokal et al. demonstrated that cubic LLZO can be formed at 700 °C [42]. However, Janai et al. reported that a more stable cubic LLZO could be obtained by adding a small amount of Al at 700 °C [43]. Hamao et al. synthesized $Li_{6.5}La_3Zr_{1.5}Ta_{0.5}O_{12}$ (LLZTO) at a considerably lower temperature of 500 °C by reacting $La_3Zr_{1.5}Ta_{0.5}O_{8.75}$ with Li_2O as the precursor powder via solid-state sintering [48]. They also demonstrated that dense LLZTO sheets can be fabricated at a low temperature of 700 °C by reacting the precursor $La_3Zr_{1.5}Ta_{0.5}O_{8.75}$ sintered at 1600 °C with a $LiNO_3$ vapor phase [49]. Recently, Guo et al. reported that LiOH and $La_3Zr_{1.5}Ta_{0.5}O_{8.75}$ reacted to form LLZTO, and dense LLZTO was prepared by sintering at 1100 °C for 2 h [50].

Previous reports suggested that dense LLZTO ceramics can be directly produced at low temperatures using dense precursor pellets. Therefore, in this study, we synthesized densified LLZTO ceramics by

* Corresponding author.
E-mail address: KUWATA.Naoaki@nims.go.jp (N. Kuwata).

https://doi.org/10.1016/j.ssi.2023.116408
Received 2 March 2023; Received in revised form 4 August 2023; Accepted 9 November 2023
Available online 24 November 2023

Table 1
Previous reports on liquid phase sintering for the preparation of LLZO pellets.

Solid electrolyte	Conductivity ($S \cdot cm^{-1}$)	E_a (eV)	Additive	Sintering temperature	Reference
$Li_7La_3Zr_2O_{12}$	3.00×10^{-4} at 25 °C	0.28	Al_2O_3	1100 °C	[21]
$Li_7La_3Zr_2O_{12}$	2.00×10^{-4} at RT	–	$Al(NO_3)_3 \cdot 9H_2O$	1200 °C	[23]
$Li_{6.5}La_3Zr_{1.5}Ta_{0.5}O_{12}$	4.90×10^{-4} at RT	0.38	γ-Al_2O_3	1100 °C	[24]
$Li_7La_3Zr_2O_{12}$	4.26×10^{-4} at 25 °C	–	Li_2O-Al_2O_3-SiO_2	1150 °C	[31]
$Li_{6.8}La_{2.95}Ca_{0.05}Zr_{1.75}Nb_{0.25}O_{12}$	3.60×10^{-4} at 25 °C	0.32	Al_2O_3 and Li_3BO_3	790 °C	[34]
Al doped $Li_7La_3Zr_2O_{12}$	1.90×10^{-5} at RT	–	Li_3BO_3	900 °C	[37]
Al doped $Li_7La_3Zr_2O_{12}$	1.00×10^{-4} at 30 °C	0.36	Li_3BO_3	900 °C	[38]
$Li_{6.4}La_3Zr_{1.4}Ta_{0.6}O_{12}$	5.47×10^{-4} at 30 °C	–	Li_3BO_3	1000 °C	[39]
$Li_{6.55}La_{2.95}Ca_{0.05}Zr_{1.5}Ta_{0.5}O_{12}$	1.33×10^{-4} at 30 °C	0.39	Li_3BO_3	800 °C	[40]
$Li_7La_3ZrNbO_{12}$	7.98×10^{-7} at 30 °C	–	LiOH	900 °C	[41]
$Li_7La_3ZrNbO_{12}$	2.52×10^{-5} at 30 °C	0.32	BaO-B_2O_3-SiO_2-CaO-Al_2O_3	900 °C	[41]
$Li_7La_3ZrNbO_{12}$	7.78×10^{-5} at 30 °C	0.39	LiO_2-B_2O_3-SiO_2-CaO-Al_2O_3	900 °C	[41]

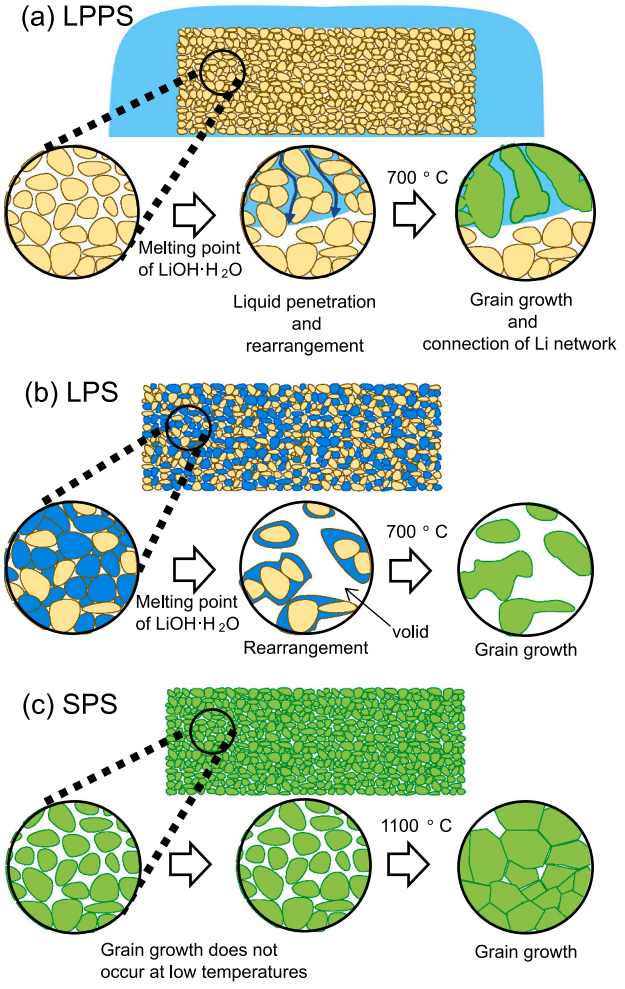

Fig. 1. Process of making LLZTO pellets by (a)LPPS, (b)LPS and (c)SPS method.

directly reacting precursor pellets with a lithium hydroxide melt (LPPS). In addition, precursor pellets were prepared by pressurization only without sintering. The ionic conductivities, microstructures, and densities of the prepared LLZTO samples were analyzed. The low-temperature densification mechanism of the LPPS method is discussed and compared with those of the SPS and LPS methods.

2. Experimental

2.1. Synthesis of precursor powder

The precursor powder, $La_3Zr_{1.5}Ta_{0.5}O_{8.75}$, was synthesized via a solid-state reaction. $La(OH)_3 \cdot H_2O$ (99.9%, Fujifilm Wako Pure Chemical Corporation), ZrO_2 (99.0%, Tosoh Corporation), and Ta_2O_5 (99.9%, Fujifilm Wako Pure Chemical Corporation) were weighed in stoichiometric ratios and ball milled in hexane at 400 rpm for 6 h. The powder was pressed at 100 MPa to form pellets and then sintered at 1200 °C for 12 h at a heating rate of 10 °C·min^{-1}. Sintering was conducted in an air atmosphere using an MgO plate.

2.2. Synthesis of garnet-type $Li_{6.5}La_3Zr_{1.5}Ta_{0.5}O_{12}$ by LPS

The following two methods were used to prepare pellets using reactive LPS. The first method was LPPS. The precursor $La_3Zr_{1.5}Ta_{0.5}O_{8.75}$ powder was uniaxially compressed at 6.25 MPa and then isostatically pressed at 200 MPa for 5 min to prepare a green body with a diameter of 10 mm. The prepared pellets were placed in a magnesia crucible, mixed with lithium hydroxide monohydrate ($LiOH \cdot H_2O$, 99.0%, Wako Pure Chemical Industries, Ltd.) in a molar ratio of 8:1, and sintered between 500 °C and 900 °C for 40 h. This method is named liquid-phase penetration sintering (LPPS) (Fig. 1a) because the liquid phase penetrates the precursor pellets from the outside.

The second method was the conventional LPS method. The precursor $La_3Zr_{1.5}Ta_{0.5}O_{8.75}$ powder and $LiOH \cdot H_2O$ were mixed. An excess of 10 wt% $LiOH \cdot H_2O$ was added to compensate for Li loss during the heating process. The mixed powder was ball-milled with hexane and zirconia balls for 6 h at 400 rpm using a planetary mill and then dried at 80 °C. The powder was uniaxially compressed at 6.25 MPa and isostatically pressed at 200 MPa for 5 min to produce a green body with a diameter of 10 mm. To suppress Li evaporation, the pellets were coated with the main powder (mixed powder of $La_3Zr_{1.5}Ta_{0.5}O_{8.75}$ and $LiOH \cdot H_2O$) and sintered in the atmosphere of 500–1150 °C for 40 h. In the LPS method, the Li source exists inside the pellet, whereas in the LPPS method, it penetrates the pellet from the outside (Fig. 1b). The LPPS, LPS, and SPS methods are illustrated in Fig. 1.

2.3. Synthesis of garnet-type $Li_{6.5}La_3Zr_{1.5}Ta_{0.5}O_{12}$ by solid phase sintering

For comparison with the LPPS and LPS methods, garnet-type $La_3Zr_{1.5}Ta_{0.5}O_{8.75}$ pellets were also produced using the conventional SPS method. The $La_3Zr_{1.5}Ta_{0.5}O_{8.75}$ powder was mixed with $LiOH \cdot H_2O$ in a molar ratio of 1:6.5. An excess of 10 wt% $LiOH \cdot H_2O$ was added to compensate for Li loss during the heating process. The precursor powder was milled with hexane and zirconia balls for 6 h at 400 rpm using a planetary mill and then dried at 80 °C. The powder was uniaxially pressed at 100 MPa into pellets and calcined at 900 °C for 12 h at a heating rate of 10 °C min^{-1}. Solid-state sintering was conducted under an air atmosphere on a magnesia plate. The synthesized LLZTO powder was uniaxially compressed at 6.25 MPa and then isostatically pressed at 200 MPa for 5 min to produce a green body with a diameter of 10 mm. In order to suppress Li evaporation, the green bodies were coated with the main (LLZTO) powder and sintered in air at 500–1150 °C for 40 h

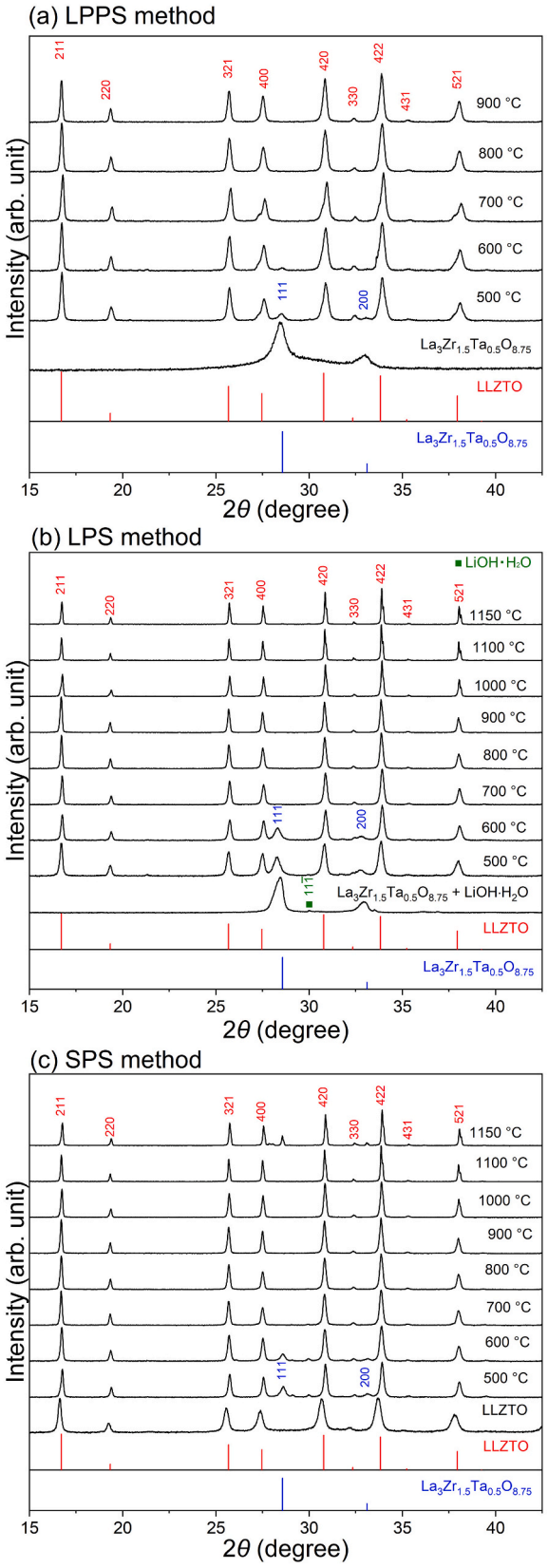

Fig. 2. X-ray diffraction pattern of the samples prepared by (a)LPPS, (b)LPS and (c)SPS method. Reflections from fluorite-type $La_3Zr_{1.5}Ta_{0.5}O_{8.75}$ and garnet-type $Li_{6.5}La_3Zr_{1.5}Ta_{0.5}O_{12}$ are labelled with Miller indices coloured in red and blue, respectively. (For interpretation of the references to colour in this figure legend, the reader is referred to the web version of this article.)

(Fig. 1c).

2.4. Characterization

X-ray diffraction (XRD) patterns of powder samples were obtained using an X-ray diffractometer (MiniFlex 600, Rigaku) machine in the range of $2\theta = 10°–80°$ at a scanning rate of $3°\ min^{-1}$ with a Cu-$K_\alpha$radiation. Li:La:Zr:Ta atomic ratios were measured using inductively coupled plasma optical emission spectroscopy (5800 ICP-OES, Agilent). The microstructures of the sintered pellets were analyzed using scanning electron microscopy (SEM; VE-8800, KEYENCE and JSM-7800F, JEOL Ltd.). Elemental analysis was performed using energy-dispersive X-ray spectroscopy (EDS) coupled with SEM. The ionic conductivity was measured using impedance spectroscopy. Li-ion-blocking Au electrodes were sputtered onto both surfaces of the sintered pellets after they were polished with sandpaper (#400). The impedance spectra were collected using a high-frequency impedance measurement system (E4990A Impedance Analyzer, Keysight Technologies, Inc.). The frequency range was 100 MHz −20 Hz and the AC amplitude was 10 mV. The temperature dependence of the ionic conductivities was measured in the range of −50 °C to 50 °C. Non-blocking electrode cells with a Li/LLZTO/Li configuration were prepared to evaluate the critical current density and Li/LLZTO interface resistance. Thin-film Li electrodes were prepared by vacuum thermal evaporation of lithium metal on both sides of the LLZTO pellets. Charging and discharging were performed for 10 min at each current density for 11 cycles. The SEM morphologies of the sintered bodies were investigated on cross sections prepared by Ar ion milling using a cross-section polisher (CP, IB-09020CP, JEOL) and a mechanical polisher (IS-POLIDHER ISPP-1000, Ikegami Seiki Co.). Secondary ion mapping was performed using a time-of-flight secondary-ion mass spectrometer (TOF-SIMS5, ION-TOF). A mapping analysis was performed using a Bi_3^{++} primary ion beam operating at 60 keV and 0.5 pA. The mapping area was $100 \times 100\ \mu m^2$ with a spatial resolution of 254 × 254 pixels. The measurement area was pre-sputtered using an O_2^+ beam at 1 keV.

3. Results and discussion

3.1. Crystal structure

Fig. 2(a) shows XRD patterns of the LPPS samples sintered between 500 °C and 900 °C. The precursor powder, $La_3Zr_{1.5}Ta_{0.5}O_{8.75}$, had a fluorite-type structure. The overall XRD pattern of the precursor, $La_3Zr_{1.5}Ta_{0.5}O_{8.75}$ is also illustrated in Fig. S1 in Supplementary Information. The lattice constant is 5.42 Å. The XRD patterns of fluorite-type $La_3Zr_{1.5}Ta_{0.5}O_{8.75}$ [48] and pyrochlore-type $La_2Zr_2O_7$ [51] were very similar. Based on its compositional identity, the precursor powder was attributed to a fluorite-type structure. The melted $LiOH{\cdot}H_2O$ permeated and reacted with the $La_3Zr_{1.5}Ta_{0.5}O_{8.75}$ pellets to form garnet-type $Li_{6.5}La_3Zr_{1.5}Ta_{0.5}O_{12}$ as shown in Eq. (1). The sample diffraction peaks sintered at a low temperature of 500 °C can be assigned to garnet-type LLZTO. This suggests that $La_3Zr_{1.5}Ta_{0.5}O_{8.75}$ reacted with molten LiOH since the melting point of $LiOH{\cdot}H_2O$ is 450 °C, which is expressed as Eq. (1).

$$La_3Zr_{1.5}Ta_{0.5}O_{8.75} + 6.5LiOH{\cdot}H_2O \rightarrow Li_{6.5}La_3Zr_{1.5}Ta_{0.5}O_{12} + 9.75H_2O\uparrow \quad (1)$$

The XRD patterns for LPPS samples exhibited shoulder peaks on the left side, especially at 700 °C. Owing to the excess LiOH in the LPPS method, H_2O may have been formed by the partial decomposition of LiOH. Consequently, partial proton exchange may occur in LLZTO. The left-sided shoulder peaks can be explained by Li^+/proton exchange with a larger lattice constant. Above 800 °C, the XRD patterns of the LPPS sample showed a single phase of the cubic LLZTO. [48]

Fig. 2(b) shows XRD patterns of the LPS samples sintered at 500–1150 °C. Similar to the illustration in Fig. 2(a), a structural change from fluorite-type to cubic garnet was observed in the LPS pellets.

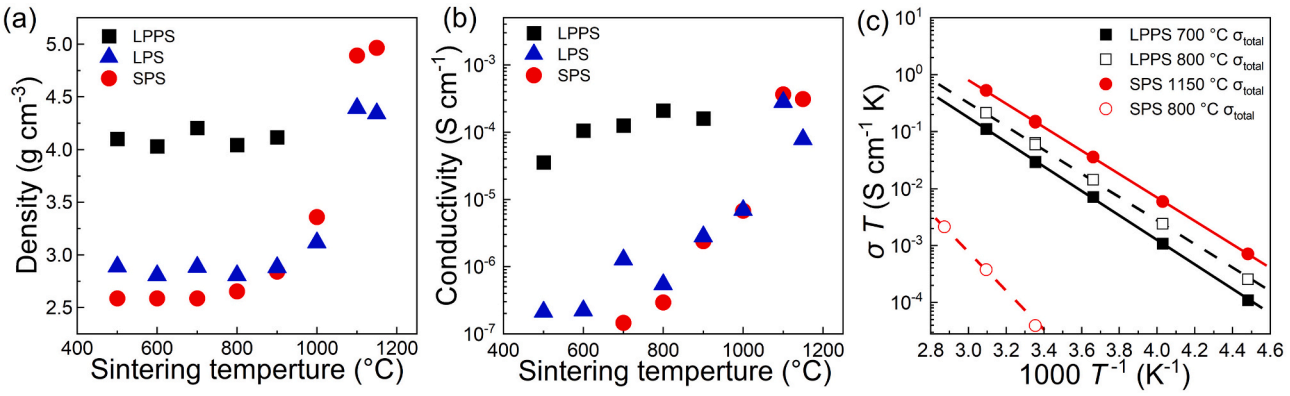

Fig. 3. (a) Density and (b) conductivity of LLZTO prepared at sintering temperatures of 500–1150 °C. (c) Arrhenius plot for total conductivity of the LLZTO sample measured using Au/LLZO/Au blocking electrodes.

Fig. 2(c) shows XRD patterns of the SPS samples sintered at 500–1150 °C. Because cubic garnet-type LLZTO powder was synthesized and then sintered into pellets, the dominant diffractions in all the patterns can be assigned to LLZTO. As the sintering temperature increased, the diffraction lines narrowed, owing to the enhanced crystallinity of LLZTO. Although the powder used for the SPS method is LLZTO, diffractions from fluorite-type $La_3Zr_{1.5}Ta_{0.5}O_{8.75}$ are observed in the XRD patterns at 500 °C and 600 °C. The formation of $La_3Zr_{1.5}Ta_{0.5}O_{8.75}$ is due to the partial decomposition of the proton exchanged LLZTO at 500 °C [45,47,52]. In the SPS method, the starting material (LLZTO) is partially proton-exchanged because it is stored in air. Proton exchange also occurs during LLZTO regrind. Therefore, a decomposition reaction occurs at 500 °C, resulting in $La_3Zr_{1.5}Ta_{0.5}O_{8.75}$ and H_2O. Then again at 700 °C, $La_3Zr_{1.5}Ta_{0.5}O_{8.75}$ reacts with excess Li_2O (from the covered LLZTO powder) to form LLZTO [12]. For the LPS and LPPS methods, the starting materials (LZTO and LiOH·H_2O) were stable in air. Thus, proton exchange does not occur when stored in the open atmosphere. The lattice constants of the synthesized LLZTO are as follows: $a = 12.93$ Å by LPPS at 800 °C, $a = 12.93$ Å by LPS at 1150 °C, and $a = 12.94$ Å by SPS at 1150 °C. The lattice constant of the LPPS sample is slightly smaller than that for single crystals, a = 12.9455 Å, reported by Kataoka et al. [53].

3.2. Density and ionic conductivity

Fig. 3(a) shows the densities of the samples prepared using LPPS, LPS, and SPS as functions of the sintering temperature. The density was calculated from the external dimensions and masses of the pellets. The densities of the samples prepared using SPS and LPS are <3.0 g cm^{-3} between 500 and 700 °C, then increase rapidly above 800 °C. The density of the SPS sample was 5.0 g cm^{-3} at 1100 °C. The theoretical density of LLZTO is 5.4 g cm^{-3}; therefore, the relative density of this sample is 92.5%. The difference in the densities of the LPS and SPS pellets was small. In the LPS method, pellets are formed from a mixed powder comprising $La_3Zr_{1.5}Ta_{0.5}O_{8.75}$ and LiOH·H_2O, where LiOH·H_2O occupies 58% by volume. Therefore, large voids remained between the LLZTO grains, preventing densification by capillary action.

In contrast, the LPPS sample is denser than 4.0 g cm^{-3} even at a low sintering temperature of 500 °C. The pellets were densified by penetration of the liquid phase from the outside. In the LPPS method, only $La_3Zr_{1.5}Ta_{0.5}O_{8.75}$ is used to form pellets; therefore, the distance

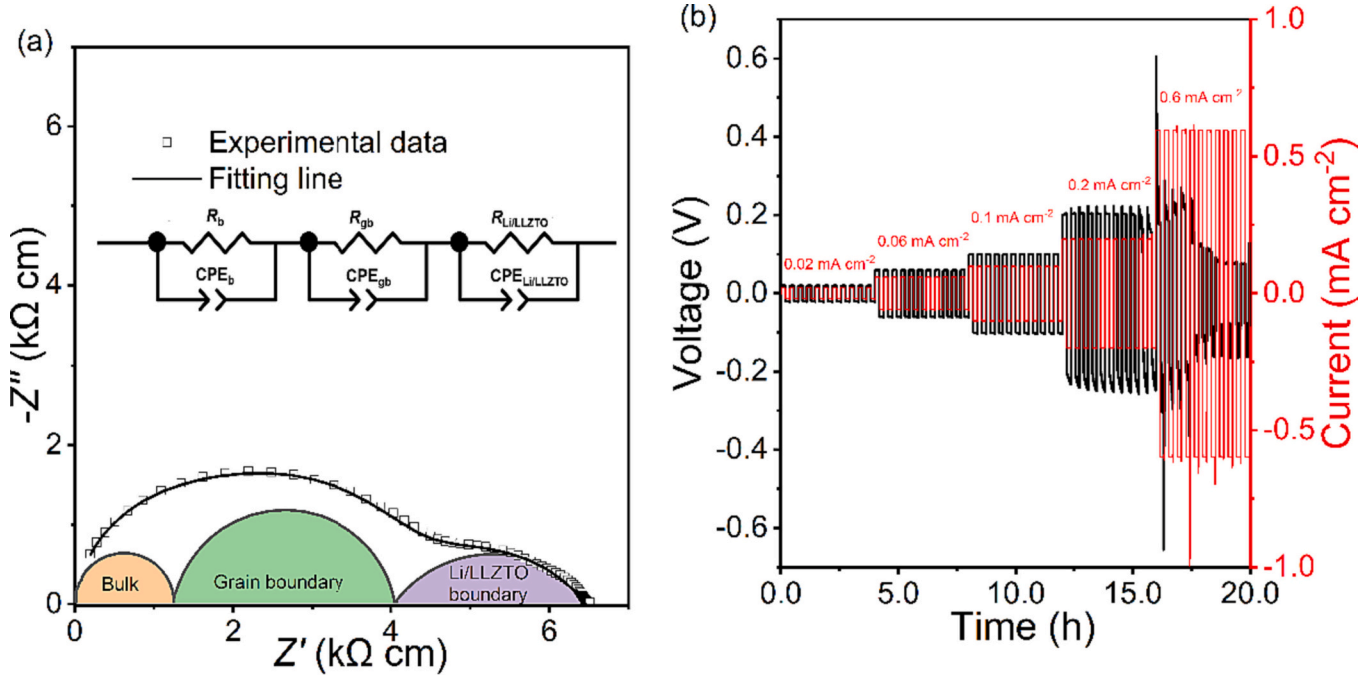

Fig. 4. (a) Complex impedance plot and (b) direct current polarization curve of LLZTO prepared by the LPPS method using the Li/LLZTO/Li symmetric cell.

Table 2
R_b, R_{gb} and $R_{Li/LLZTO}$ for LLZTO prepared by the LPPS method.

T (°C)	R_b (Ω cm)	R_{gb} (Ω cm)	$R_{Li/LLZTO}$ (Ω cm)
25	1250	2801	2459

between the particles is sufficiently small for capillary action to occur. For the chemical reactions shown in Eq. (1) to proceed only Li and O must diffuse into the interior of the $La_3Zr_{1.5}Ta_{0.5}O_{8.75}$ grains, which maintains the pellet shape. The diffusion of Li and O is rapid enough because the reaction proceeds through the pellet even at a low temperature of 500 °C.

Fig. 3(b) shows the ionic conductivity of the samples prepared by LPS, LPPS, and SPS at 25 °C. In the SPS method, the ionic conductivity increases gradually from a sintering temperature of 700–1000 °C and abruptly at 1100 °C, reaching the maximum value of 4×10^{-4} S cm^{-1}. In the LPS method, the ionic conductivity increases rapidly between 1000 and 1100 °C and reaches a maximum ionic conductivity of 2×10^{-4} S cm^{-1} at a sintering temperature of 1100 °C. In contrast, the LPPS samples show ionic conductivities higher than 1×10^{-4} S cm^{-1} even at low sintering temperatures from 600 °C to 900 °C. An exceptionally high ionic conductivity of 2×10^{-4} S cm^{-1} is achieved at 800 °C. The ionic conductivity and density were comparable between the LPS and SPS methods and were significantly improved by the LPPS method.

Fig. 3(c) shows the Arrhenius plots of ionic conductivity in the temperature range of −50 °C to 50 °C for the samples prepared by LPPS and SPS. The total ionic conductivities, including the bulk and grain boundary contributions, are shown in Fig. 3c. The lithium-ion conductivity (σ) was determined using the Arrhenius equation:

$$\sigma T = \sigma_0 exp\left(-\frac{E_a}{k_B T}\right), \quad (2)$$

where σ_0 is a preexponential factor, E_a is the activation energy, k_B is the Boltzmann constant (1.381×10^{-23} J K^{-1}), and T is the absolute temperature. The conductivities of all the samples were linear with respect to the T^{-1} function, indicating that the ionic conduction pathways were unchanged over the measured temperature range. The activation energies of the LLZTO pellets prepared at 700 °C and 800 °C by the LPPS method and LLZTO pellets prepared by the SPS method at 1150 °C are 0.41 to 0.42 eV, respectively, which are consistent with the values in previous reports [24,54–56]. On the other hand, LLZTO pellets prepared by the SPS method at 800 °C exhibit a very high activation energy (0.7 eV).

To evaluate the resistance of the Li/LLZTO interface, a Li/LLZTO/Li symmetric cell was created using Li thin films deposited on both sides of the sample. Fig. 4(a) shows a complex impedance plot of the LLZTO prepared by the LPPS method at 800 °C. The impedance plot was normalized by multiplying a factor of $A\ l^{-1}$, where, A and l are the

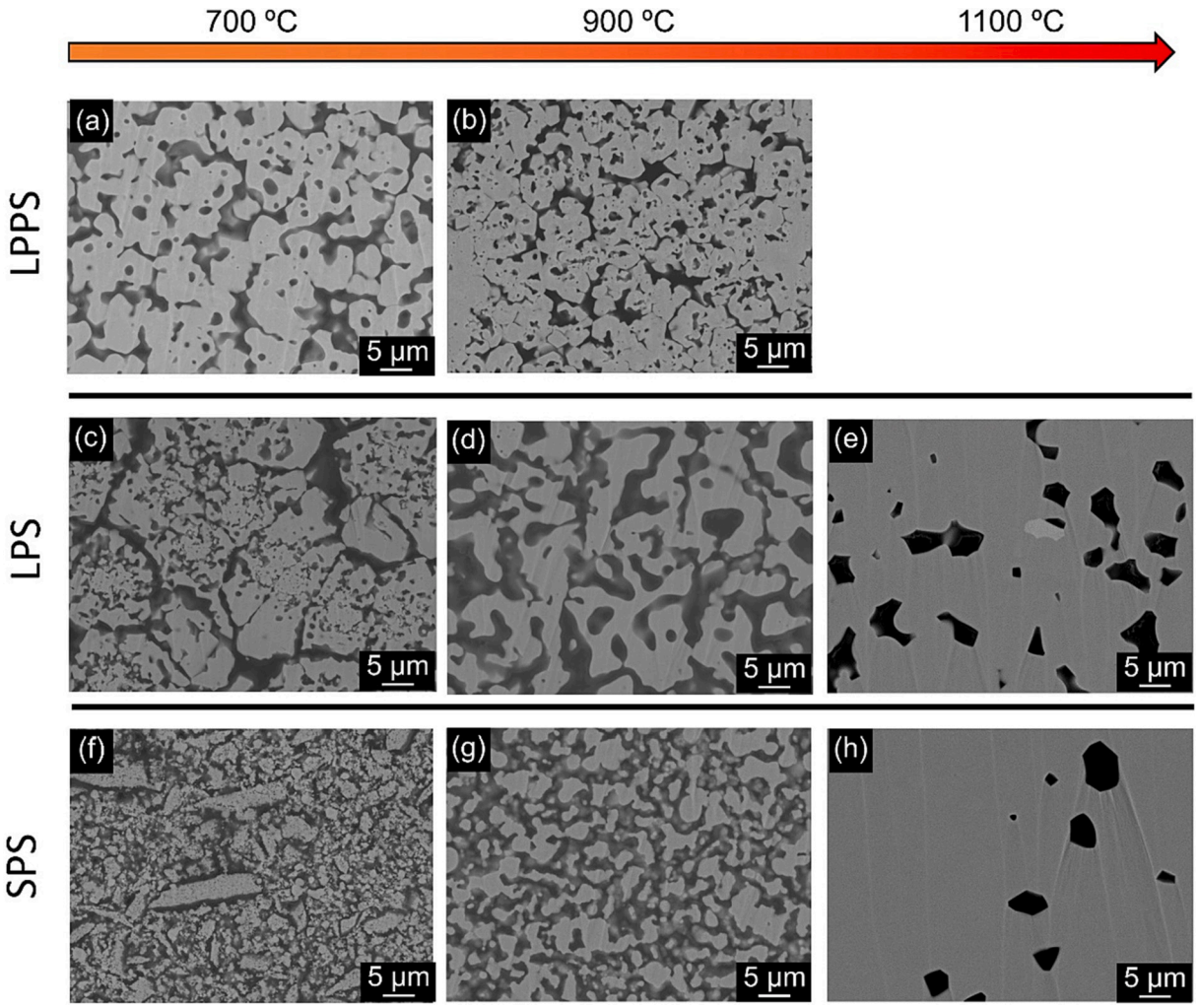

Fig. 5. Cross-sectional SEM images of LLZTO pellets fabricated using the LPPS method at (a) 700 °C and (b) 900 °C. Cross-sectional SEM images of LLZTO pellets fabricated using the LPS method at (c) 700 °C, (d) 900 °C, and (e) 1100 °C. Cross-sectional SEM images of the LLZTO pellets fabricated using the SPS method at (f) 700 °C, (g) 900 °C, and (h) 1100 °C.

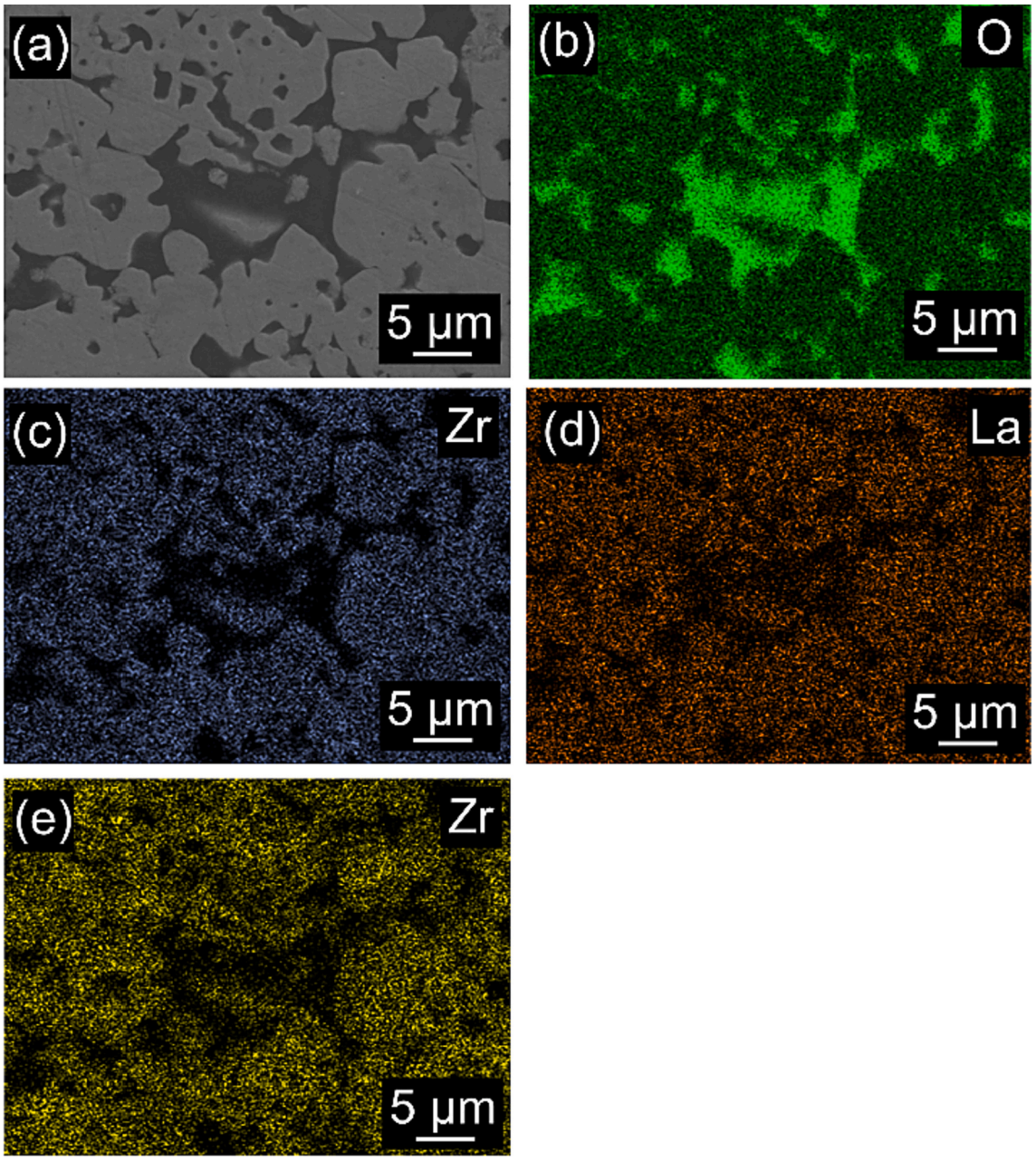

Fig. 6. EDS mapping images of LLZTO fabricated via liquid phase sintering. (a) Mapping area, (b) O, (c) Zr, (d) La, and (e) Ta.

surface area and thickness of the pellet, respectively. Complex impedance plots for polycrystalline ion-conducting ceramics with Li electrodes usually consist of three semicircles corresponding to the intraparticle (bulk, R_b), intergranular (grain boundaries, R_{gb}), and Li/LLZTO interface ($R_{Li/LLZTO}$) resistances. However, the two semicircles resulting from the bulk and grain boundary elements are not well separated in this sample. Similar behavior has been observed for other garnet-type lithium-ion conductors [5,15,23,28,39,57]. To obtain the bulk and grain boundary resistances, the equivalent circuit is shown in the inset of Fig. 4(a), where CPE, a constant phase element for each component, was fitted to the experimental data. Table 2 presents the resistance values separated by the fitting line. The resistance of the Li/LLZTO interface was lower than that of LLZTO.

The critical current density was investigated to characterize the stability of the LLZTO/Li interface. Fig. 4(b) shows direct current cycling of the Li/LLZTO/Li symmetric cell at room temperature. The relationship between the cell voltage and current density followed Ohm's law up to a current density of 0.2 mA cm^{-2} and deviates at a current density of 0.6 mA cm^{-2}. The critical current density was comparable to that of dense LLZTO pellets prepared using high-temperature sintering [58]. Introducing additives such as LiOH, Li_2CO_3, Li_3PO_4, Li_3BO_3, and lithium halides effectively reduces pores by suppressing the formation of Li dendrites [59–63]. Similarly, the pellets prepared by the LPPS also suppress the formation of Li dendrites by filling the pores with $LiOH{\cdot}H_2O$.

3.3. Cross-sectional morphology

The cross-sectional SEM images shown in Fig. 5(a)–(h) show the difference in grain structures of the samples prepared using LPPS, LPS, and SPS methods. The grain growth of the LLZTO pellets prepared via SPS increased after 900 °C, as shown in Fig. 5(f)–(h). The particles grew rapidly at 1100 °C, and the sintered bodies became extremely dense. In contrast, as shown in Fig. 5(a), LLZTO particles in the pellets prepared

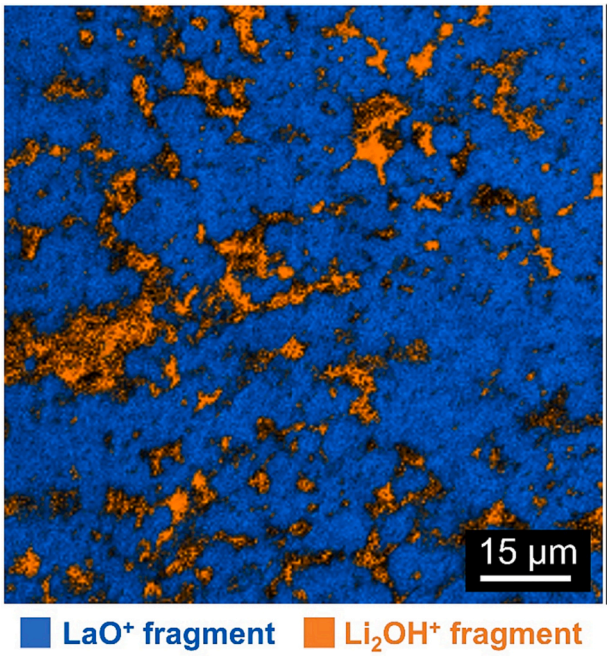

Fig. 7. Local fragment distribution of LaO^+ (blue) and Li_2OH^+(orange) fragments for LLZTO pellets using liquid phase sintering. (For interpretation of the references to colour in this figure legend, the reader is referred to the web version of this article.)

Table 3
Elemental contents of the sintered samples measured by ICP-OES. The ratios are normalized with respect to the La content.

	Li	La	Zr	Ta
$La_3Zr_{1.5}Ta_{0.5}O_{8.75}$ prepared by solid phase reaction method	0.00	3.00	1.50	0.50
LLZTO prepared at 800° C by the LPPS	10.45	3.00	1.51	0.50
LLZTO prepared at 1150° C by the SPS	6.40	3.00	1.48	0.49

by LPPS grew, even at 700 °C. This microstructure contributes to high ionic conductivity at low sintering temperatures. In the sample prepared by LPS, as shown in Fig. 5(c) to (e), grain growth progresses from 700 °C to 1100 °C. However, as shown in Fig. 5(d), many voids exist between the LLZTO particles to form an insufficiently connected structure, even at 900 °C.

Fig. 6 depicts cross-sectional SEM-EDS images of the sample prepared with LPPS at 800 °C. The La, Ta, and Zr distributions indicate that the light-gray areas in Fig. 6a are LLZTO particles. The dark gray areas between the LLZTO particles only contain O and are free of La, Zr, and Ta. In contrast, only reflections from LLZTO are detected in the XRD pattern in Fig. 2(a), suggesting that these intergrain regions comprise amorphous phases. To investigate the composition of the intergrain phase, high-resolution TOF-SIMS imaging was performed on a cross-section of the pellet.

Fig. 7 shows a TOF-SIMS image of a pellet prepared using LPPS at 800 °C. TOF-SIMS enables the simultaneous analysis of a large number of fragments. For simplicity, the image focused on the LaO^+ and Li_2OH^- fragments. The Li_2OH^- distribution is indicative of LLZTO particles, and LaO^+ shows the same distribution as ZrO^+, which is consistent with the SEM-EDS results. In contrast, the Li^+ and Li_2OH^+ fragments are present in the intergrain region. Therefore, the intergrain phase was concluded to be amorphous LiOH. Further, Fig. S2 illustrates the scanning transmission electron microscopy and electron energy-loss spectroscopy (EELS) results of the grain boundary phase between the LLZTO of the sample prepared by LPPS at 800 °C. The EELS pattern of the intergrain

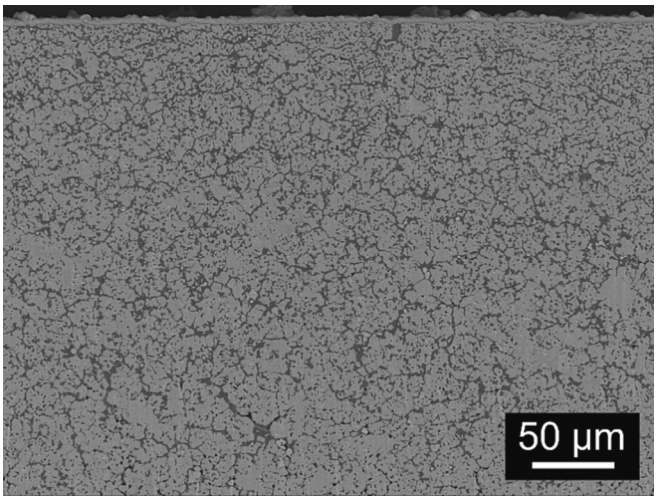

Fig. 8. Cross-sectional SEM images of the pellets fabricated via LPPS at 800 °C.

phase was similar to that of LiOH, but not to that of lithium carbonate. The melting point of LiOH was 475 °C under atmospheric pressure, and the dehydration of LiOH into Li_2O with associated H_2O departure occurred at 477–577 °C [64]. In the LPPS method, the sintering temperature is higher than the dehydration temperature, ranging from 500 °C to 900 °C for 40 h. In the present method, dehydration may be more difficult than under atmospheric pressure because LiOH is confined to the grain boundaries and no gas-phase H_2O is generated.

Table 3 summarizes the results of ICP-OES analysis for three samples: the precursor material $La_3Zr_{1.5}Ta_{0.5}O_{8.75}$ powder, LLZTO prepared by LPPS at 800 °C, and LLZTO prepared by SPS at 1150 °C. The elemental ratios in Table 3 are normalized with respect to a La content of 3. The ICP results of $La_3Zr_{1.5}Ta_{0.5}O_{8.75}$ are in excellent agreement with its stoichiometric composition. The Zr and Ta atomic ratios in the LLZTO prepared using LPPS and SPS also agreed with the designed elemental ratios. Conversely, the Li content of LLZTO prepared by LPPS at 800 °C is 10.45, which is considerably higher than that of the stoichiometry of LLZTO (6.5). This can be attributed to the amorphous LiOH component between the LLTO grains. Based on the ICP-OES results, the theoretical density of the LLZTO and LiOH composite was 4.3 g cm^{-3}. Conversely, the experimental density of the pellets prepared by LPPS at 800 °C is 4.0 g cm^{-3}, indicating that the LPPS provides very dense LLZTO pellets with a relative density of 93% at 800 °C.

The volume ratio of the LLZTO component in the composite pellet obtained from the ICP-OES analysis was 71%. Considering the relative density of 93%, the volume ratio of LLZTO in the pellets was 66%. Compared to pellets prepared by SPS at 1000 °C, where the relative density of LLZTO was similar (62%), the ionic conductivity of the LPPS pellets was >10 times higher. Since the ionic conductivity of LiOH is very low (1×10^{-9} S cm^{-1} at 150 °C) [65], it was assumed that LiOH did not contribute to the ionic conduction in the pellet prepared by LPPS. This suggests that LLZTO prepared by LPPS provides an excellent conduction pathway for Li^+ ions. As seen in the cross-section of the LPPS pellets, the network structures formed by the coarse LLZTO particles support ionic conduction (Fig. 8).

As shown in Fig. 1(a), the liquid phase permeates from the outside into the pellet, in which the precursor particles are in close contact with each other, such that the permeating LiOH melt forms a continuous LLZTO network from the outside of the pellet. This continuous network formation of coarse particles establishes a continuous pathway for lithium-ion conduction, resulting in high ionic conductivity.

4. Conclusions

In this study, dense garnet-type LLZTO ceramics with good ionic

conduction were prepared at low temperatures (500–900 °C) via LPPS. Grain growth and interactions proceeded using the $La_3Zr_{1.5}Ta_{0.5}O_{8.75}$ precursor and $LiOH{\cdot}H_2O$ melt to provide Li conduction pathways. The pellet prepared using LPPS at 800 °C exhibited an ionic conductivity of 2×10^{-4} S cm^{-1}. SEM-EDS and TOF-SIMS measurements revealed that the LLZTO particles connected to form a conduction network for lithium ions with high ionic conductivity in the presence of amorphous LiOH.

Author contributions

Naoki Yoshida: Investigation, methodology, visualization, and writing of the original draft. Naoaki Kuwata: Methodology, project administration, writing, review, and editing. Gen Hasegawa: TOF-SIMS investigation. Kazunori Takada: conceptualization, supervision, writing, review, and editing. All authors have read and agreed to the published version of the manuscript.

Declaration of Competing Interest

There are no conflicts to declare.

Data availability

Data will be made available on request.

Acknowledgments

This work was supported by Materials Processing Science project (“Materealize”) of MEXT [grant numbers JPMXP0219207397]. This study was supported by the JST ALCA-SPRING (Specially Promoted Research for Innovative Next Generation Batteries) project [grant number JPMJAL1301]. The cross-sectional polishing, TOF-SIMS, and SEM-EDS measurements were performed using the National Institute for Materials Science Battery Research Platform. This study was also supported by JSPS KAKENHI [grant number 21H02033].

References

[1] R. Murugan, V. Thangadurai, W. Weppner, Fast lithium ion conduction in garnet-type $Li_7La_3Zr_2O_{12}$, Angew. Chem. Int. Ed. 46 (2007) 7778–7781, https://doi.org/10.1002/anie.200701144.

[2] J. Awaka, N. Kijima, H. Hayakawa, J. Akimoto, Synthesis and structure analysis of tetragonal $Li_7La_3Zr_2O_{12}$ with the garnet-related type structure, J. Solid State Chem. 182 (2009) 2046–2052, https://doi.org/10.1016/j.jssc.2009.05.020.

[3] M. Huang, T. Liu, Y. Deng, H. Geng, Y. Shen, Y. Lin, C.W. Nan, Effect of sintering temperature on structure and ionic conductivity of $Li_{7-x}La_3Zr_2O_{12-0.5x}$ (x = 0.5~0.7) ceramics, Solid State Ionics 204–205 (2011) 41–45, https://doi.org/10.1016/j.ssi.2011.10.003.

[4] M. Kotobuki, H. Munakata, K. Kanamura, Y. Sato, T. Yoshida, Compatibility of $Li_7La_3Zr_2O_{12}$ solid electrolyte to all-solid-state battery using Li metal anode, J. Electrochem. Soc. 157 (2010) A1076, https://doi.org/10.1149/1.3474232.

[5] Y. Li, C.A. Wang, H. Xie, J. Cheng, J.B. Goodenough, High lithium ion conduction in garnet-type $Li_6La_3ZrTaO_{12}$, Electrochem. Commun. 13 (2011) 1289–1292, https://doi.org/10.1016/j.elecom.2011.07.008.

[6] S. Ohta, T. Kobayashi, T. Asaoka, High lithium ionic conductivity in the garnet-type oxide $Li_{7-X}La_3(Zr_{2-X},Nb_X)O_{12}$ (X = 0–2), J. Power Sources 196 (2011) 3342–3345, https://doi.org/10.1016/j.jpowsour.2010.11.089.

[7] K.H. Kim, Y. Iriyama, K. Yamamoto, S. Kumazaki, T. Asaka, K. Tanabe, C.A. J. Fisher, T. Hirayama, R. Murugan, Z. Ogumi, Characterization of the interface between $LiCoO_2$ and $Li_7La_3Zr_2O_{12}$ in an all-solid-state rechargeable lithium battery, J. Power Sources 196 (2011) 764–767, https://doi.org/10.1016/j.jpowsour.2010.07.073.

[8] Y. Ren, T. Liu, Y. Shen, Y. Lin, C.W. Nan, Chemical compatibility between garnet-like solid state electrolyte $Li_{6.75}La_3Zr_{1.75}Ta_{0.25}O_{12}$ and major commercial lithium battery cathode materials, J. Mater. 2 (2016) 256–264, https://doi.org/10.1016/j.jmat.2016.04.003.

[9] T. Kato, T. Hamanaka, K. Yamamoto, T. Hirayama, F. Sagane, M. Motoyama, Y. Iriyama, In-situ $Li_7La_3Zr_2O_{12}/LiCoO_2$ interface modification for advanced all-solid-state battery, J. Power Sources 260 (2014) 292–298, https://doi.org/10.1016/j.jpowsour.2014.02.102.

[10] E.A. Il’ina, B.D. Antonov, M.I. Vlasov, Stability investigations of composite solid electrolytes based on $Li_7La_3Zr_2O_{12}$ in contact with $LiCoO_2$, Solid State Ionics 356 (2020), 115452, https://doi.org/10.1016/j.ssi.2020.115452.

[11] G. Vardar, W.J. Bowman, Q. Lu, J. Wang, R.J. Chater, A. Aguadero, R. Seibert, J. Terry, A. Hunt, I. Waluyo, D.D. Fong, A. Jarry, E.J. Crumlin, S.L. Hellstrom, Y. M. Chiang, B. Yildiz, Structure, chemistry, and charge transfer resistance of the Interface between $Li_7La_3Zr_2O_{12}$ electrolyte and $LiCoO_2$ cathode, Chem. Mater. 30 (2018) 6259–6276, https://doi.org/10.1021/acs.chemmater.8b01713.

[12] J. Wakasugi, H. Munakata, K. Kanamura, Thermal stability of various cathode materials against $Li_{6.25}Al_{0.25}La_3Zr_2O_{12}$ electrolyte, Electrochemistry. 85 (2017) 77–81, https://doi.org/10.5796/electrochemistry.85.77.

[13] J. Sastre, X. Chen, A. Aribia, A.N. Tiwari, Y.E. Romanyuk, Fast charge transfer across the $Li_7La_3Zr_2O_{12}$ solid electrolyte/$LiCoO_2$ cathode Interface enabled by an interphase-engineered all-thin-film architecture, ACS Appl. Mater. Interfaces 12 (2020) 36196–36207, https://doi.org/10.1021/acsami.0c09777.

[14] S. Uhlenbruck, J. Dornseiffer, S. Lobe, C. Dellen, C.L. Tsai, B. Gotzen, D. Sebold, M. Finsterbusch, O. Guillon, Cathode-electrolyte material interactions during manufacturing of inorganic solid-state lithium batteries, J. Electroceram. 38 (2017) 197–206, https://doi.org/10.1007/s10832-016-0062-x.

[15] V. Thangadurai, W. Weppner, Investigations on electrical conductivity and chemical compatibility between fast lithium ion conducting garnet-like $Li_6BaLa_2Ta_2O_{12}$ and lithium battery cathodes, J. Power Sources 142 (2005) 339–344, https://doi.org/10.1016/j.jpowsour.2004.11.001.

[16] K. Park, B.C. Yu, J.W. Jung, Y. Li, W. Zhou, H. Gao, S. Son, J.B. Goodenough, Electrochemical nature of the cathode interface for a solid-state Lithium-ion battery: interface between $LiCoO_2$ and garnet-$Li_7La_3Zr_2O_{12}$, Chem. Mater. 28 (2016) 8051–8059, https://doi.org/10.1021/acs.chemmater.6b03870.

[17] L. Miara, A. Windmüller, C.L. Tsai, W.D. Richards, Q. Ma, S. Uhlenbruck, O. Guillon, G. Ceder, About the compatibility between high voltage spinel cathode materials and solid oxide electrolytes as a function of temperature, ACS Appl. Mater. Interfaces 8 (2016) 26842–26850, https://doi.org/10.1021/acsami.6b09059.

[18] E.A. Il’ina, A.A. Raskovalov, Studying of superionic solid electrolyte $Li_7La_3Zr_2O_{12}$ stability by means of chemical thermodynamics for application in all-solid-state batteries, Electrochim. Acta 330 (2020), 135220, https://doi.org/10.1016/j.electacta.2019.135220.

[19] H. Aono, E. Sugimoto, Y. Sadaoka, N. Imanaka, G.-Y. Adachi, Electrical property and sinterability of $LiTi_2(PO_4)_3$ mixed with lithium salt (Li_3PO_4 or Li_3BO_3), Solid State Ionics 47 (1991) 257–264, https://doi.org/10.1016/0167-2738(91)90247-9.

[20] J.H. Ahn, S.Y. Park, J.M. Lee, Y. Park, J.H. Lee, Local impedance spectroscopic and microstructural analyses of Al-in-diffused $Li_7La_3Zr_2O_{12}$, J. Power Sources 254 (2014) 287–292, https://doi.org/10.1016/j.jpowsour.2013.12.115.

[21] H. El-Shinawi, G.W. Paterson, D.A. MacLaren, E.J. Cussen, S.A. Corr, Low-temperature densification of Al-doped $Li_7La_3Zr_2O_{12}$: a reliable and controllable synthesis of fast-ion conducting garnets, J. Mater. Chem. A 5 (2017) 319–329, https://doi.org/10.1039/c6ta06961d.

[22] Y. Li, T. Yang, W. Wu, Z. Cao, W. He, Y. Gao, J. Liu, G. Li, Effect of Al-Mo codoping on the structure and ionic conductivity of sol-gel derived $Li_7La_3Zr_2O_{12}$ ceramics, Ionics. 24 (2018) 3305–3315, https://doi.org/10.1007/s11581-018-2497-3.

[23] Y. Jin, P.J. McGinn, Al-doped $Li_7La_3Zr_2O_{12}$ synthesized by a polymerized complex method, J. Power Sources 196 (2011) 8683–8687, https://doi.org/10.1016/j.jpowsour.2011.05.065.

[24] Y. Wang, P. Yan, J. Xiao, X. Lu, J.G. Zhang, V.L. Sprenkle, Effect of Al_2O_3 on the sintering of garnet-type $Li_{6.5}La_3Zr_{1.5}Ta_{0.5}O_{12}$, Solid State Ionics 294 (2016) 108–115, https://doi.org/10.1016/j.ssi.2016.06.013.

[25] Y. Ren, H. Deng, R. Chen, Y. Shen, Y. Lin, C.W. Nan, Effects of Li source on microstructure and ionic conductivity of Al-contained $Li_{6.75}La_3Zr_{1.75}Ta_{0.25}O_{12}$ ceramics, J. Eur. Ceram. Soc. 35 (2015) 561–572, https://doi.org/10.1016/j.jeurceramsoc.2014.09.007.

[26] P. Badami, S. Smetaczek, A. Limbeck, D. Rettenwander, C.K. Chan, A.N.M. Kannan, Facile synthesis of Al-stabilized lithium garnets by a solution-combustion technique for all solid-state batteries, Mater. Adv. 2 (2021) 5181–5188, https://doi.org/10.1039/d1ma00393c.

[27] S. Kumazaki, Y. Iriyama, K.H. Kim, R. Murugan, K. Tanabe, K. Yamamoto, T. Hirayama, Z. Ogumi, High lithium ion conductive $Li_7La_3Zr_2O_{12}$ by inclusion of both Al and Si, Electrochem. Commun. 13 (2011) 509–512, https://doi.org/10.1016/j.elecom.2011.02.035.

[28] P. Badami, J. Mark Weller, A. Wahab, G. Redhammer, L. Ladenstein, D. Rettenwander, M. Wilkening, C.K. Chan, A.N.M. Kannan, Highly conductive garnet-type electrolytes: access to $Li_{6.5}La_3Zr_{1.5}Ta_{0.5}O_{12}$ prepared by molten salt and solid-state methods, ACS Appl. Mater. Interfaces 12 (2020) 48580–48590, https://doi.org/10.1021/acsami.0c14056.

[29] C.A. Geiger, E. Alekseev, B. Lazic, M. Fisch, T. Armbruster, R. Langner, M. Fechtelkord, N. Kim, T. Pettke, W. Weppner, Crystal chemistry and stability of “$Li_7La_3Zr_2O_{12}$” garnet: a fast lithium-ion conductor, Inorg. Chem. 50 (2011) 1089–1097, https://doi.org/10.1021/ic101914e.

[30] E. Yi, W. Wang, J. Kieffer, R.M. Laine, Key parameters governing the densification of cubic-$Li_7La_3Zr_2O_{12}$ Li^+ conductors, J. Power Sources 352 (2017) 156–164, https://doi.org/10.1016/j.jpowsour.2017.03.126.

[31] Y. Tang, Q. Zhang, Z. Luo, P. Liu, A. Lu, Effects of Li_2O-Al_2O_3-SiO_2 system glass on the microstructure and ionic conductivity of $Li_7La_3Zr_2O_{12}$ solid electrolyte, Mater. Lett. 193 (2017) 251–254, https://doi.org/10.1016/j.matlet.2017.01.134.

[32] S. Qin, X. Zhu, Y. Jiang, M. Ling, Z. Hu, J. Zhu, Growth of self-textured Ga^{3+}-substituted $Li_7La_3Zr_2O_{12}$ ceramics by solid state reaction and their significant enhancement in ionic conductivity, Appl. Phys. Lett. 112 (2018), https://doi.org/10.1063/1.5019179.

[33] P. Zhao, Y. Wen, J. Cheng, G. Cao, Z. Jin, H. Ming, Y. Xu, X. Zhu, A novel method for preparation of high dense tetragonal $Li_7La_3Zr_2O_{12}$, J. Power Sources 344 (2017) 56–61, https://doi.org/10.1016/j.jpowsour.2017.01.088.

[34] S. Ohta, J. Seki, Y. Yagi, Y. Kihira, T. Tani, T. Asaoka, Co-sinterable lithium garnet-type oxide electrolyte with cathode for all-solid-state lithium ion battery, J. Power Sources 265 (2014) 40–44, https://doi.org/10.1016/j.jpowsour.2014.04.065.

[35] R.H. Shin, S.I. Son, S.M. Lee, Y.S. Han, Y. Do Kim, S.S. Ryu, Effect of Li_3BO_3 additive on densification and ion conductivity of garnet-type $Li_7La_3Zr_2O_{12}$ solid electrolytes of all-solid-state lithium-ion batteries, J. Korean Ceram. Soc. 53 (2016) 712–718, https://doi.org/10.4191/kcers.2016.53.6.712.

[36] S.V. Pershina, E.A. Il'Ina, O.G. Reznitskikh, Phase composition, density, and ionic conductivity of the $Li_7La_3Zr_2O_{12}$-based composites with $LiPO_3$ glass addition, Inorg. Chem. 56 (2017) 9880–9891, https://doi.org/10.1021/acs.inorgchem.7b01379.

[37] R. Takano, K. Tadanaga, A. Hayashi, M. Tatsumisago, Low temperature synthesis of Al-doped $Li_7La_3Zr_2O_{12}$ solid electrolyte by a sol-gel process, Solid State Ionics 255 (2014) 104–107, https://doi.org/10.1016/j.ssi.2013.12.006.

[38] K. Tadanaga, R. Takano, T. Ichinose, S. Mori, A. Hayashi, M. Tatsumisago, Low temperature synthesis of highly ion conductive $Li_7La_3Zr_2O_{12}$-Li_3BO_3 composites, Electrochem. Commun. 33 (2013) 51–54, https://doi.org/10.1016/j.elecom.2013.04.004.

[39] H. Xie, C. Li, W.H. Kan, M. Avdeev, C. Zhu, Z. Zhao, X. Chu, D. Mu, F. Wu, Consolidating the grain boundary of the garnet electrolyte LLZTO with Li_3BO_3 for high-performance $LiNi_{0.8}Co_{0.1}Mn_{0.1}O_2$/$LiFePO_4$ hybrid solid batteries, J. Mater. Chem. A 7 (2019) 20633–20639, https://doi.org/10.1039/c9ta03263k.

[40] L.C. Zhang, J.F. Yang, Y.X. Gao, X.P. Wang, Q.F. Fang, C.H. Chen, Influence of Li_3BO_3 additives on the Li^+ conductivity and stability of Ca/Ta-substituted $Li_{6.55}(La_{2.95}Ca_{0.05})(Zr_{1.5}Ta_{0.5})O_{12}$ electrolytes, J. Power Sources 355 (2017) 69–73, https://doi.org/10.1016/j.jpowsour.2017.04.044.

[41] N.C. Rosero-Navarro, T. Yamashita, A. Miura, M. Higuchi, K. Tadanaga, Effect of sintering additives on relative density and Li-ion conductivity of Nb-doped $Li_7La_3ZrO_{12}$ solid electrolyte, J. Am. Ceram. Soc. 100 (2017) 276–285, https://doi.org/10.1111/jace.14572.

[42] I. Kokal, M. Somer, P.H.L. Notten, H.T. Hintzen, Sol-gel synthesis and lithium ion conductivity of $Li_7La_3Zr_2O_{12}$ with garnet-related type structure, Solid State Ionics 185 (2011) 42–46, https://doi.org/10.1016/j.ssi.2011.01.002.

[43] N. Janani, S. Ramakumar, L. Dhivya, C. Deviannapoorani, K. Saranya, R. Murugan, Synthesis of cubic $Li_7La_3Zr_2O_{12}$ by modified sol-gel process, Ionics. 17 (2011) 575–580, https://doi.org/10.1007/s11581-011-0611-x.

[44] Y. Shimonishi, A. Toda, T. Zhang, A. Hirano, N. Imanishi, O. Yamamoto, Y. Takeda, Synthesis of garnet-type $Li_{7-x}La_3Zr_2O_{12-1/2x}$ and its stability in aqueous solutions, Solid State Ionics 183 (2011) 48–53, https://doi.org/10.1016/j.ssi.2010.12.010.

[45] M. Kotobuki, M. Koishi, Preparation of $Li_7La_3Zr_2O_{12}$ solid electrolyte via a sol-gel method, Ceram. Int. 40 (2014) 5043–5047, https://doi.org/10.1016/j.ceramint.2013.09.009.

[46] T. Yang, Z.D. Gordon, Y. Li, C.K. Chan, Nanostructured garnet-type solid electrolytes for Lithium batteries: electrospinning synthesis of $Li_7La_3Zr_2O_{12}$ nanowires and particle size-dependent phase transformation, J. Phys. Chem. C 119 (2015) 14947–14953, https://doi.org/10.1021/acs.jpcc.5b03589.

[47] T. Kimura, Y. Yamada, K. Yamamoto, T. Matsuda, H. Nomura, T. Hirayama, Rapid low-temperature synthesis of tetragonal single-phase $Li_7La_3Zr_2O_{12}$, J. Am. Ceram. Soc. 100 (2017) 1313–1319, https://doi.org/10.1111/jace.14633.

[48] N. Hamao, K. Hamamoto, N. Taguchi, S. Tanaka, J. Akimoto, Synthesis and crystal structure of fluorite-type $La_{2.4}Zr_{1.2}Ta_{0.4}O_7$: a precursor oxide for low temperature formation of garnet-type $Li_{6.5}La_3Zr_{1.5}Ta_{0.5}O_{12}$, Solid State Ionics 357 (2020), 115460, https://doi.org/10.1016/j.ssi.2020.115460.

[49] N. Hamao, Y. Yamaguchi, K. Hamamoto, Low-temperature synthesis of dense garnet-type $Li_{6.5}La_3Zr_{1.5}Ta_{0.5}O_{12}$ layered structures using fluorite-type precursor oxide, J. Alloys Compd. 865 (2021), 158223, https://doi.org/10.1016/j.jallcom.2020.158223.

[50] J. Guo, J.M. Weller, S. Yang, M.H. Bhat, C.K. Chan, Reactive sintering of garnet-type $Li_{6.4}La_3Zr_{1.4}Ta_{0.6}O_{12}$ (LLZTO) from pyrochlore precursors prepared using a non-aqueous sol–gel method, Ionics. 29 (2023) 581–590, https://doi.org/10.1007/s11581-022-04837-4.

[51] T. Hagiwara, K. Nomura, H. Yamamura, Relationship between crystal structure and oxide-ion conduction in $Nd_2Zr_2O_7$ and $La_2Zr_2O_7$ deduced by high-temperature neutron diffraction, Solid State Ionics 262 (2014) 551–554, https://doi.org/10.1016/j.ssi.2014.01.027.

[52] Y. Wang, W. Lai, Phase transition in lithium garnet oxide ionic conductors $Li_7La_3Zr_2O_{12}$: the role of ta substitution and H_2O/CO_2 exposure, J. Power Sources 275 (2015) 612–620, https://doi.org/10.1016/j.jpowsour.2014.11.062.

[53] K. Kataoka, J. Akimoto, High ionic conductor member of garnet-type oxide $Li_{6.5}La_3Zr_{1.5}Ta_{0.5}O_{12}$, ChemElectroChem. 5 (2018) 2551–2557, https://doi.org/10.1002/celc.201800679.

[54] Y. Matsuda, Y. Itami, K. Hayamizu, T. Ishigaki, M. Matsui, Y. Takeda, O. Yamamoto, N. Imanishi, Phase relation, structure and ionic conductivity of $Li_{7-x-3y}Al_yLa_3Zr_{2-x}Ta_xO_{12}$, RSC Adv. 6 (2016) 78210–78218, https://doi.org/10.1039/c6ra13317g.

[55] R. Inada, K. Kusakabe, T. Tanaka, S. Kudo, Y. Sakurai, Synthesis and properties of Al-free $Li_{7-x}La_3Zr_{2-x}Ta_xO_{12}$ garnet related oxides, Solid State Ionics 262 (2014) 568–572, https://doi.org/10.1016/j.ssi.2013.09.008.

[56] A. Dorai, N. Kuwata, R. Takekawa, J. Kawamura, K. Kataoka, J. Akimoto, Diffusion coefficient of lithium ions in garnet-type $Li_{6.5}La_3Zr_{1.5}Ta_{0.5}O_{12}$ single crystal probed by ^7Li pulsed field gradient-NMR spectroscopy, Solid State Ionics 327 (2018) 18–26, https://doi.org/10.1016/j.ssi.2018.10.016.

[57] J.H. Ahn, S.Y. Park, J.M. Lee, Y. Park, J.H. Lee, Local impedance spectroscopic and microstructural analyses of Al-in-diffused $Li_7La_3Zr_2O_{12}$, J. Power Sources 254 (2014) 287–292, https://doi.org/10.1016/j.jpowsour.2013.12.115.

[58] L. Cheng, W. Chen, M. Kunz, K. Persson, N. Tamura, G. Chen, M. Doeff, Effect of surface microstructure on electrochemical performance of garnet solid electrolytes, ACS Appl. Mater. Interfaces 7 (2015) 2073–2081, https://doi.org/10.1021/am508111r.

[59] Z. Zhang, L. Zhang, C. Yu, X. Yan, B. Xu, L. Min Wang, Lithium halide coating as an effective intergrain engineering for garnet-type solid electrolytes avoiding high temperature sintering, Electrochim. Acta 289 (2018) 254–263, https://doi.org/10.1016/j.electacta.2018.08.079.

[60] B. Xu, W. Li, H. Duan, H. Wang, Y. Guo, H. Li, H. Liu, Li_3PO_4-added garnet-type $Li_{6.5}La_3Zr_{1.5}Ta_{0.5}O_{12}$ for Li-dendrite suppression, J. Power Sources 354 (2017) 68–73, https://doi.org/10.1016/j.jpowsour.2017.04.026.

[61] R. Hongahally Basappa, T. Ito, T. Morimura, R. Bekarevich, K. Mitsuishi, H. Yamada, Grain boundary modification to suppress lithium penetration through garnet-type solid electrolyte, J. Power Sources 363 (2017) 145–152, https://doi.org/10.1016/j.jpowsour.2017.07.088.

[62] H. Duan, F. Oluwatemitope, S. Wu, H. Zheng, Y. Zou, G. Li, Y. Wu, H. Liu, Li/garnet interface optimization: an overview, ACS Appl. Mater. Interfaces 12 (2020) 52271–52284, https://doi.org/10.1021/acsami.0c16966.

[63] T. Deng, X. Ji, Y. Zhao, L. Cao, S. Li, S. Hwang, C. Luo, P. Wang, H. Jia, X. Fan, X. Lu, D. Su, X. Sun, C. Wang, J.G. Zhang, Tuning the anode–electrolyte interface chemistry for garnet-based solid-state Li metal batteries, Adv. Mater. 32 (2020) 1–10, https://doi.org/10.1002/adma.202000030.

[64] J.M. Kiat, G. Boemare, B. Rieu, D. Aymes, Structural evolution of LiOH: evidence of a solid–solid transformation toward Li_2O close to the melting temperature, Solid State Commun. 108 (1998) 241–245, https://doi.org/10.1016/S0038-1098(98)00346-9.

[65] R.T. Johnson, R.N. Biefield, J.D. Keck, Ionic conductivity in Li_5AlO_4 and LiOH, Pergamon Press. 7 (1977) 541–559, https://doi.org/10.1016/0025-5408(77)90066-6.